

Flow instabilities in thermocapillary-buoyant liquid pools

H. C. KUHLMANN† AND U. SCHOISSWOHL

Institute of Fluid Mechanics and Heat Transfer, Vienna University of Technology, Resselgasse 3,
A-1040 Vienna, Austria

(Received 9 March 2009; revised 6 October 2009; accepted 20 October 2009)

The linear stability of the incompressible axisymmetric flow in a buoyant-thermocapillary liquid pool is considered which is heated from above by a heat flux with a parabolic radial profile. Buoyancy forces and radial thermocapillary stresses due to the inhomogeneous surface temperature distribution drive a toroidal vortex. In the absence of buoyancy and for low Prandtl numbers the basic flow becomes unstable typically by a stationary centrifugal instability. At moderate Prandtl numbers the rotational symmetry is broken by hydrothermal waves. In the limit of vanishing Prandtl number two other critical modes are found if the pool is very shallow. One mode is a centrifugally destabilized rotating wave with high azimuthal wavenumber. The other mode is steady and it is driven by the deceleration of the radial inward return flow as it approaches the axis. The deceleration results from an entrainment of fluid into the thin layer of rapid radial outward surface flow. The centrifugal instability of the toroidal vortex flow is assisted by buoyancy in the low-Prandtl-number limit, because the cooling from the sidewall augments the thermocapillary driving. For moderately high Prandtl numbers a stable thermal stratification suppresses the hydrothermal-wave instabilities.

1. Introduction

Flow in non-isothermal liquid pools involving liquid–gas interfaces arises in a number of technical applications. Among these are crystal growth from the melt (Kuhlmann 1999), fusion welding (DebRoy & David 1995), electron-beam evaporation (Karcher *et al.* 2000) and casting, to name only a few. Many of these processes, fusion welding in particular, are very complex due to dynamic liquid–solid and liquid–gas interfaces, multi-component melts, surface active agents, vaporization and other specific complications such as the motion of the workpiece relative to the incident laser beam in continuous fusion welding. To better understand the physical processes of key importance for these applications model systems have been devised to study the fundamental fluid flow, unperturbed by additional complicating effects.

When the fluid motion is driven at or near the free surface by a localized heat source a cylindrical domain is the natural geometry. In pure liquids the radial variation of the surface temperature drives a significant fluid motion via the thermocapillary effect (Scriven & Sternling 1960). The flow will be axisymmetric for weak driving, but it can undergo bifurcations to three-dimensional flow for stronger driving forces, and even become turbulent (Karcher *et al.* 2000). The situation is different from the

† Email address for correspondence: hendrik.kuhlmann@tuwien.ac.at

classical Marangoni instability (Pearson 1958) of a quiescent liquid layer due to a homogeneous heat flux at the free surface.

Thermocapillary flows in cylindrical geometry have been studied for open-top cylindrical pools and annular configurations. Kamotani & Ostrach (1994) computed the axisymmetric flow due to laser-spot heating in an upright circular cylindrical container for plane and curved free-surface shapes. To eliminate buoyancy forces Kamotani, Ostrach & Masud (1999) carried out experiments under microgravity conditions onboard of the space shuttle. A cylindrical pool with a flat free surface was heated coaxially by a CO₂ laser beam with nearly Gaussian profile. The resulting axisymmetric thermocapillary flow in silicone oil ($Pr = 33$) became unstable to a three-dimensional time-dependent flow in form of an azimuthally standing wave with circumferential period of two. Motivated by these experiments Sim & Zebib (2002) computed the three-dimensional flow in a cylindrical container driven by thermocapillary forces due to an axisymmetric heat flux with a top-hat profile for $Pr = 30$ and 97 . They took into account the static deformation of the liquid–gas interface which results from a given volume of liquid assuming a fixed contact line. Azimuthally standing and travelling waves were found above a critical heat flux depending on the free surface being either flat or concave. Their results for fixed interface shapes were in qualitative agreement with the experimental findings of Kamotani *et al.* (1999). Hence, a dynamic deformability of the interface is not required for the observed three-dimensional flow instabilities.

In electron-beam evaporation the thermocapillary flow is usually much stronger than in laser heating. Karcher *et al.* (2000) carried out experiments using a shallow cylindrical container (aspect ratio $\Gamma \approx 4$) filled with iron and heated in the centre by an electron beam of up to 50 kW. For Marangoni numbers ranging from $Ma = 2 \times 10^7$ to 10^8 turbulent convection was found. In addition, the two-dimensional turbulent thermocapillary convection in a box was computed for $Pr = 0.01$ and Marangoni numbers $Ma = O(10^5)$. Both experiment and simulation yielded Nusselt numbers which approximately scaled like $Nu \sim Ma^{1/3}$. This scaling has been predicted by Pumir & Blumenfeld (1996) for turbulent thermocapillary flow in a half space driven by a point source of heat at the free surface. The exponent of 0.27 rather $1/3$ obtained from the numerics was traced back by Karcher *et al.* (2000) to the two-dimensional rather than three-dimensional simulation. Boeck & Karcher (2003) considered a model in which a liquid with $Pr = 0.1$ in a rectangular volume with aspect ratio $\Gamma = 2$ and square cross-section was heated by a central beam with an axisymmetric Gaussian profile. For sufficiently high Marangoni number they found flow oscillations in form of a standing wave. Moreover, they were able to confirm the laminar scaling $\sim Ma^{1/2}$ of the velocity magnitude and $\sim Ma^{-1/4}$ of the temperature field as predicted by Pumir & Blumenfeld (1996) for laminar flow.

The thermocapillary flow in an annular cylindrical gap where the inner and outer cylinders were at different temperatures has some similarities with the flow in cylindrical pools. While numerous studies have been carried out for a heating from the outer cylindrical wall (see e.g. Jing *et al.* 1999; Hintz, Schwabe & Wilke 2001) aiming at modelling certain aspects of the Czochralski process of crystal growth from the melt (Hurle 1994), only a few investigations are available for heating from the inner cylinder.

For terrestrial and for zero-gravity conditions Kamotani, Lee & Ostrach (1992) and Kamotani, Ostrach & Masud (2000) carried out experiments on the flow in an annular system heated from the inner cylinder which had a very small radius

compared to the outer one. For the high-Prandtl-number fluids employed and for different free-surface shapes they found the onset of three-dimensional flow in form of travelling waves with azimuthal period two for both gravity conditions. The free-surface temperature fields were similar to those of the waves observed in the laser-heated pool (Kamotani *et al.* 1999). The annular-gap experiment of Schwabe, Zebib & Sim (2003) carried out under conditions of weightlessness had a radius ratio of two. For relatively shallow liquid layers, realized by a movable bottom, with $Pr = 6.84$ they found an axisymmetric flow consisting of a concentric multi-roll structure similar as predicted for rectangular geometries by Villers & Platten (1992). For larger temperature differences Schwabe *et al.* (2003) found azimuthally standing waves which were traced back to the hydrothermal waves in infinite layers (Smith & Davis 1983). In a subsequent paper Sim, Zebib & Schwabe (2003) carried out corresponding simulations and established a qualitative agreement with the experiments of Schwabe *et al.* (2003). Heat loss from the free surface was invoked to explain the remaining differences. To study the effect of the free-surface shape Sim, Kim & Zebib (2004) computed the two-dimensional thermocapillary convection in an open cylindrical annulus heated from the inner wall. For $Pr = 30$ they confirmed earlier results of Sim & Zebib (2002) and established that dynamic free-surface deformations do not lead to oscillatory two-dimensional flow for the parameters considered, just as for the pool geometry.

To date, little is known about the instabilities in thermocapillary liquid pools where the motion is driven by a central hot spot and the dependence of the critical conditions on the governing parameters. The present paper is aimed at the linear stability of the steady axisymmetric flow in open cylindrical pools and the dependence of the critical Reynolds number, frequency and wavenumber on the geometry, Prandtl number and strength of buoyancy. To that end we define a model with a minimum of parameters in §2. There we also present the methods of investigation and the solution strategy. Section 3 deals with the verification and grid convergence of the numerical methods employed. Results are presented in §4. We consider in detail the dependence of the basic flow and its linear stability on the Prandtl number, aspect ratio and buoyancy level. Particular attention is paid to the physical mechanisms by which the basic flow is destabilized. The results are summarized in §5 and discussed in comparison with experiments for solutocapillary flow in shallow dishes.

2. Statement of the problem

2.1. Governing equations

We consider an incompressible Newtonian liquid of density ρ and kinematic viscosity ν occupying an upright circular cylinder of height d and radius R . The aspect ratio is $\Gamma = R/d$. The liquid volume is bounded laterally and from below by solid walls of constant temperature. The top boundary is a free liquid–gas interface which is exposed to a vertical heat flux (figure 1). Such a heat flux could be due to, e.g. laser irradiation the energy being absorbed within a very thin surface layer. The imposed heat flux induces temperature variations in the liquid volume and at the free surface giving rise to buoyant and thermocapillary forces, respectively, which drive a fluid flow. Employing cylindrical coordinates (r, φ, z) the non-dimensional Boussinesq

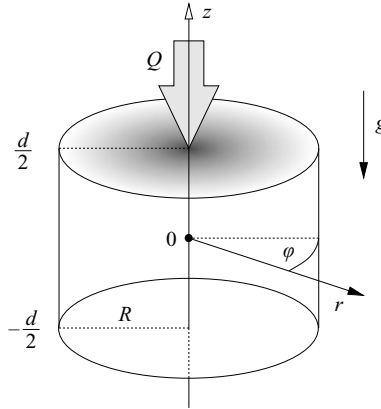


FIGURE 1. Geometry and coordinate system.

approximation of the Navier–Stokes equations reads

$$\left(\frac{\partial}{\partial t} + \mathbf{U} \cdot \nabla \right) \mathbf{U} = -\nabla P + \nabla^2 \mathbf{U} + Gr T \mathbf{e}_z, \quad (2.1a)$$

$$Pr \left(\frac{\partial}{\partial t} + \mathbf{U} \cdot \nabla \right) T = \nabla^2 T, \quad (2.1b)$$

$$\nabla \cdot \mathbf{U} = 0, \quad (2.1c)$$

where $\mathbf{U} = (U, V, W)^T$, P and T denote the velocity vector, pressure and temperature fields, Gr is the Grashof number, Pr the Prandtl number and \mathbf{e}_z the axial unit vector. The acceleration of gravity g is acting in the negative z direction. In (2.1) we have used the length, velocity, time, pressure and temperature scales d , v/d , d^2/ν , $\rho v^2/d^2$ and ΔT , respectively, the latter of which still needs to be defined.

At the bottom and the mantle of the cylinder we assume no-slip, no-penetration and constant-temperature boundary conditions

$$\mathbf{U}(r, \varphi, z = -1/2) = \mathbf{U}(r = \Gamma, \varphi, z) = 0, \quad (2.2a)$$

$$T(r, \varphi, z = -1/2) = T(r = \Gamma, \varphi, z) = 0, \quad (2.2b)$$

where the temperature is measured relative to the wall temperature.

We consider the limit in which capillary forces dominate normal stresses at the free surface (see e.g. Sen & Davis 1982). In thermocapillary flows the relative importance of both forces is given by the Capillary number $Ca = \gamma \Delta T / \sigma$, where $\gamma \Delta T$ is the magnitude of the temperature-induced surface-tension variations with γ being the negative surface-tension coefficient. In the asymptotic limit $Ca \rightarrow 0$ static and dynamic deformations of the free surface are absent and the top free surface remains flat. This limit is a good approximation for a number of thermocapillary flows at criticality in which $Ca \approx 10^{-3} \dots 10^{-1}$ (see e.g. table 2 of Kuhlmann & Nienhüser 2002).

To minimize the governing parameters we consider an axisymmetric heat-flux-density distribution at $z = 1/2$ with a parabolic profile $Q(r)$ which vanishes at the rim $r = \Gamma$. Given $Q_{max} = Q(r = 0)$ we define the temperature scale $\Delta T = Q_{max} d / k$, where k is the thermal conductivity of the liquid. With this scaling the thermal boundary condition on the free surface at $z = 1/2$ becomes

$$\frac{\partial T}{\partial z} = Q(r) = - \left(1 - \frac{r}{\Gamma} \right)^2. \quad (2.3)$$

Neglecting viscous stresses in the ambient gas the stress balance at the flat non-deformable liquid–gas interface requires (see e.g. Kuhlmann 1999)

$$\mathbf{S} \cdot \mathbf{e}_z + Re(\mathbf{I} - \mathbf{e}_z \mathbf{e}_z) \cdot \nabla T = 0, \quad (2.4)$$

where $\mathbf{S} = \nabla \mathbf{U} + (\nabla \mathbf{U})^T$ is the viscous stress tensor in the liquid phase and \mathbf{I} the identity matrix. The strength of the thermocapillary effect is determined by the thermocapillary Reynolds number Re which, together with the remaining governing parameters, is defined as

$$Re = \frac{\gamma \Delta T d}{\rho \nu^2} = \frac{\gamma Q_{max} d^2}{\rho \nu^2 k}, \quad Gr = \frac{\beta \Delta T g d^3}{\nu^2}, \quad Pr = \frac{\nu}{\kappa}, \quad (2.5)$$

where κ is the thermal diffusivity and β the thermal expansion coefficient at constant pressure.

A useful integral quantity characterizing the flow is the Nusselt number

$$Nu = \frac{Q_0}{Q_{cond}(\bar{T})} = \frac{\bar{T}_0}{\bar{T}}, \quad (2.6)$$

where Q_0 is the total heat flux through the free surface, \bar{T} the mean surface temperature for a given convective flow state and $Q_{cond}(\bar{T})$ the conductive heat flux that would be required to obtain the same mean surface temperature \bar{T} . Owing to the linearity of the heat conduction equation Nu can be expressed through the mean surface temperature \bar{T}_0 of the conductive state under the heat flux Q_0 .

2.2. The basic flow and its linear stability

The symmetries of the problem allow a steady axisymmetric basic flow $(\mathbf{u}_0, p_0, \theta_0)^T$ for which $\partial_t = \partial_\varphi = v_0 \equiv 0$. The basic state must satisfy the boundary conditions

$$\frac{\partial u_0}{\partial z} = -Re \frac{\partial \theta_0}{\partial r} \quad \text{and} \quad \frac{\partial \theta_0}{\partial z} = -\left(1 - \frac{r}{R}\right)^2 \quad (2.7)$$

on the free surface and $(u_0, w_0, \theta_0) = (0, 0, 0)$ on the rigid walls.

The stability of the basic state is investigated by a linear-stability analysis. To that end we decompose the full three-dimensional flow into

$$(\mathbf{U}, P, T)^T = (\mathbf{u}_0, p_0, \theta_0)^T + (\mathbf{u}, p, \theta)^T. \quad (2.8)$$

Substitution into (2.1) and linearization with respect to the perturbation quantities $(\mathbf{u}, p, \theta)^T$ yields

$$\frac{\partial \mathbf{u}}{\partial t} + \mathbf{u} \cdot \nabla \mathbf{u}_0 + \mathbf{u}_0 \cdot \nabla \mathbf{u} = -\nabla p + \nabla^2 \mathbf{u} + Gr \theta \mathbf{e}_z, \quad (2.9a)$$

$$\frac{\partial \theta}{\partial t} + \mathbf{u} \cdot \nabla \theta_0 + \mathbf{u}_0 \cdot \nabla \theta = Pr^{-1} \nabla^2 \theta, \quad (2.9b)$$

$$\nabla \cdot \mathbf{u} = 0. \quad (2.9c)$$

The perturbations must vanish on the rigid walls $(\mathbf{u}, \theta) = (0, 0)$. At the free surface we require adiabatic conditions for the perturbations, i.e. $\partial \theta / \partial z = 0$ on $z = 1/2$, and the velocity perturbations must satisfy the thermocapillary stress conditions

$$\frac{\partial u}{\partial z} = -Re \frac{\partial \theta}{\partial r} \quad \text{and} \quad \frac{\partial v}{\partial z} = -\frac{Re}{r} \frac{\partial \theta}{\partial \varphi}. \quad (2.10)$$

The solution of (2.9) is a superposition of normal modes

$$\begin{pmatrix} \mathbf{u} \\ p \\ \theta \end{pmatrix} (r, \varphi, z, t) = \begin{pmatrix} \hat{\mathbf{u}} \\ \hat{p} \\ \hat{\theta} \end{pmatrix} (r, z) e^{\lambda t} e^{im\varphi} + \text{c.c.}, \quad (2.11)$$

where m is an integer azimuthal wavenumber and $\lambda = \sigma + i\omega$ with growth rate σ and oscillation frequency ω . Using the ansatz (2.11) the discretization of (2.9) leads to the generalized eigenvalue problem

$$\mathbf{A} \cdot \mathbf{x}_k = \lambda_k \mathbf{B} \cdot \mathbf{x}_k, \quad (2.12)$$

with K eigenvectors \mathbf{x}_k and eigenvalues λ_k , where K is the size of the system. \mathbf{A} and \mathbf{B} are the matrix representations of the differential operators and boundary conditions. Note that the boundary conditions on the axis $r=0$ for the amplitudes $(\hat{\mathbf{u}}, \hat{p}, \hat{\theta})$ depend on the wavenumber m (see e.g. Xu & Davis 1984).

2.3. Energy budget of linear perturbations

For a physical understanding of the dynamics of the linear perturbations we consider the transfer rates of kinetic and thermal energy between the basic state $(\mathbf{u}_0, p_0, \theta_0)^T$ and the normal modes $(\mathbf{u}, p, \theta)^T$. The rate of change of kinetic energy \dot{E}_{kin} of the perturbation is governed by the Reynolds–Orr equation. On the margin of stability $\dot{E}_{kin} = 0$. Hence, the Reynolds–Orr equation normalized by the viscous dissipation reads

$$\frac{1}{D} \frac{dE_{kin}}{dt} = \frac{1}{D} \frac{d}{dt} \int_V \frac{\mathbf{u}^2}{2} dV = -1 + I_v + M + I_{Gr} = 0, \quad (2.13)$$

where

$$D = \int_V (\nabla \times \mathbf{u})^2 dV \quad (2.14)$$

is the rate of viscous dissipation and

$$I_v = -\frac{1}{D} \int_V \mathbf{u} \cdot [(\mathbf{u} \cdot \nabla) \mathbf{u}_0] dV \quad (2.15)$$

represents the normalized energy production by advection of basic-state momentum \mathbf{u}_0 by the perturbation flow \mathbf{u} . The quantities

$$M_r = \frac{1}{D} \int_S u \partial_z u dS, \quad M_\varphi = \frac{1}{D} \int_S v \partial_z v dS \quad \text{and} \quad I_{Gr} = \frac{Gr}{D} \int_V w \theta dV \quad (2.16)$$

represent the normalized work done by Marangoni forces acting on the free surface S in radial and azimuthal direction, $M = M_r + M_\varphi$, and the work done by buoyancy forces, respectively.

In a similar way a *thermal energy* E_{th} can be defined. For neutral stability it satisfies

$$\frac{1}{D_T} \frac{dE_{th}}{dt} = \frac{1}{D_T} \frac{d}{dt} \int_V \frac{\theta^2}{2} dV = -1 + I_T = 0. \quad (2.17)$$

Here

$$D_T = \frac{1}{Pr} \int_V (\nabla \theta)^2 dV \quad \text{and} \quad I_T = -\frac{1}{D_T} \int_V \theta (\mathbf{u} \cdot \nabla) \theta_0 dV \quad (2.18)$$

are the rate of heat diffusion and the normalized thermal energy production, respectively. It should be noted that a term $H = D_T^{-1} Pr^{-1} \int_S \theta (\partial \theta / \partial z) dS$ arises in the thermal energy budget representing the rate of change of thermal energy by a heat flux

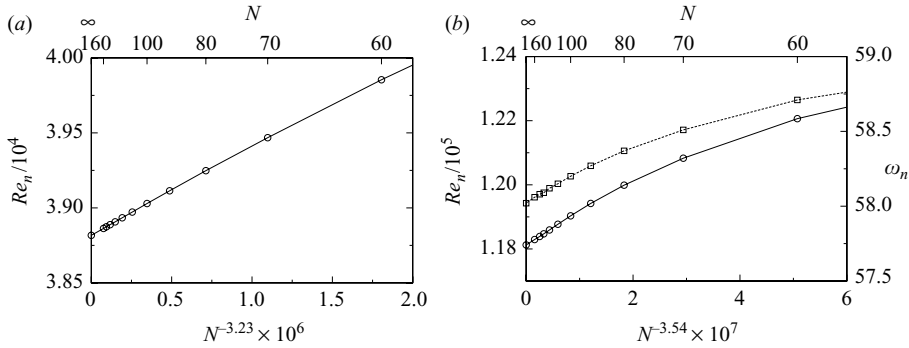


FIGURE 2. Neutral Reynolds numbers Re_n (full lines, circles) for $\Gamma = 1$, $Gr = 0$, $m = 3$ and $Pr = 0.0316$ (a) and $Pr = 3.98$ (b) as functions of the grid resolution, where $N = N_r = N_z$. The neutral frequency ω_n for $Pr = 3.98$ is shown as dashed line and squares in (b).

through the free surface. It vanishes, however, for perturbations subject to the present adiabatic boundary conditions at the free surface S . Note that the advection with the basic flow of momentum and heat $\mathbf{u}[(\mathbf{u}_0 \cdot \nabla)\mathbf{u}]/D$ and $\theta[(\mathbf{u}_0 \cdot \nabla)\theta]/D_T$, respectively, are non-zero locally, but energy preserving in the integral sense.

While (2.13) and (2.17) describe the total energy budgets, the local rates of change of energy, i.e. the densities of the rates of change of energy, are given by the respective integrands. They will be denoted, henceforth, by lower case letters, e.g. $i_v = -\mathbf{u} \cdot [(\mathbf{u} \cdot \nabla)\mathbf{u}_0]/D$.

3. Numerical solution and code verification

The basic state is computed from the two-dimensional version of (2.1) subject to boundary conditions (2.7) using primitive variables and finite volumes on a staggered grid. The resulting system of difference equations is solved by Newton–Raphson iteration employing an efficient linear systems solver from the mathematical subroutine library LAPACK.

The perturbation equations (2.9) are discretized on the same grid. Once the basic state is obtained, the generalized eigenvalue problem (2.12) is solved using inverse power iteration with shift (Golub & van Loan, 1989). Neutral stability boundaries are characterized by a vanishing growth rate $\sigma_k = \sigma(Re, Pr, Gr, \Gamma, m, k) = 0$. To find the neutral-stability hypersurfaces $Re = Re_n(Pr, Gr, \Gamma, m, k)$ the roots of σ are searched for by means of the secant method. Typically, Re is varied and the basic-state calculation as well as the eigensystem solution are carried out repeatedly. The critical Reynolds number $Re_c(Pr, Gr, \Gamma) := \min_{m,k} Re_n(Pr, Gr, \Gamma, m, k)$ is finally obtained as the minimum envelope of the neutral Reynolds numbers.

All calculations have been carried out using with a resolution of $N_r \times N_z$ grid points. In order to resolve the developing boundary layers the grid is compressed towards the free surface and the sidewall with stretching factors $\delta_r = \delta_z = 0.98$.

Since no validation data are available for the present problem, we adapted the boundary conditions to suit the half-zone problem of thermocapillary flow in an adiabatic cylindrical liquid bridge (Kuhlmann 1999). Good to excellent agreement is obtained for the basic-state and the critical data. In addition to this verification of the discretization of the bulk equations, we carried out grid-convergence studies for the open-pool problem. The results for two representative cases are shown in figure 2.

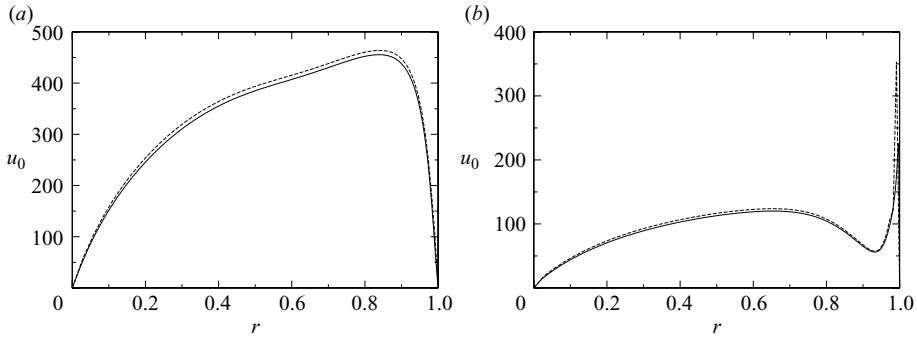


FIGURE 3. Radial velocity u_0 of the basic flow at the free surface for $Pr=0.0316$ (a) under critical conditions and $Pr=3.98$ (b) for neutral conditions. In both cases $\Gamma=1$ and $Gr=0$. Full and dashed lines indicate resolutions $N_r \times N_z = 120 \times 120$ and 60×60 , respectively, on a stretched grid.

It can be seen that grid convergence is obtained. The extrapolated values and the convergence order p were calculated by Richardson extrapolation using three grids with resolutions 90×90 , 120×120 and 160×160 .

Owing to the large number of computations to be performed for parametric studies we used a resolution of 70×70 in all subsequent calculations for reasons of computational economy. This resolution leads to a relative error for Re_n of about 2% or better in most case. Only for very large aspect ratios the error may increase up to 5%. The same accuracy holds for the integral energy budget, e.g. $|\delta E_{kin}| \leq 5\%$ or better, where δE_{kin} denotes the error in the normalized Reynolds–Orr equation (2.13).

It should be noted that the current temperature scale $\Delta T = Q_{max}d/k$ results in relatively high thermocapillary Reynolds numbers, because the associated velocity scale $\gamma Q_{max}d/(\rho\nu k)$ under estimates the magnitude of the velocity field in the liquid. From the radial velocity distributions of the basic flow under critical conditions ($m=3$) shown in figure 3(a) for $Pr=0.0316$ we find the maximum surface velocity $u_0^* = 455.4$ at $r^* = 0.841$ ($N_r \times N_z = 120 \times 120$). This yields a critical Reynolds number based on u_0^* of $Re_c^* = 455.4$ and a corresponding Marangoni number of $Ma_c^* = 14.4$. For $Pr=3.98$ the mode $m=3$ (figure 3b) is only neutral. We obtain $u_0^* = 120.1$ at $r^* = 0.655$ resulting in $Re_n^* = 120.1$ and $Ma_n^* = 478.0$. Here, we have ignored the narrow velocity peak close to the cold wall for $Pr=3.98$. These velocity-based critical Reynolds numbers are of the same order of magnitude as for related surface-force-driven systems (Schimmel, Albensoeder & Kuhlmann 2005). The maximum of the basic-state temperature difference along the free surface cannot be used as a control parameter here, because it is part of the solution and can only be obtained *a posteriori*.

4. Results and discussion

The parameter dependence of the basic flow, its instability and the physical mechanisms cannot be covered completely. Therefore, we present calculation along certain cuts through the parameter space made of Re , Pr , Γ and Gr . To study the Prandtl number dependence of the critical Reynolds number we consider a unit aspect ratio and zero gravity. Thereafter, the dependence of Re_c on the aspect ratio will be investigated for three different Prandtl numbers and $Gr=0$. Finally, the effect of buoyancy is considered for unit aspect ratio and two representative Prandtl numbers.

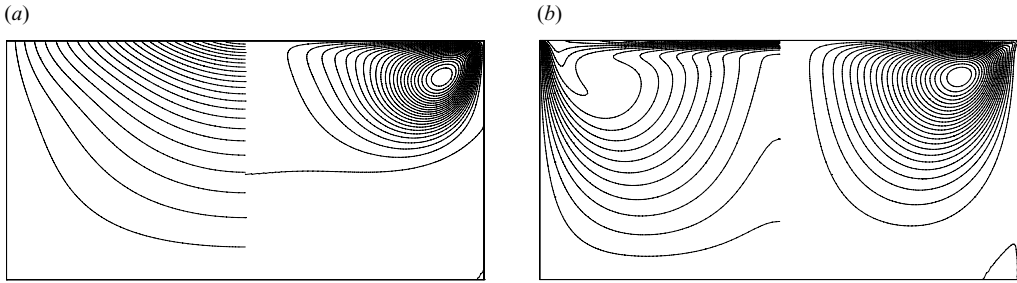


FIGURE 4. Stream function ψ_0 (right side) and isotherms θ_0 (left side) of the basic state in the (r, z) plane for (a) $Pr = 0.03$ at $Re_c = 3.88 \times 10^4$ ($Nu = 0.963$) and for (b) $Pr = 4$ at $Re_c = 1.10 \times 10^5$ ($Nu = 4.86$), both for $\Gamma = 1$ and $Gr = 0$. The flow is clockwise.

4.1. Prandtl number dependence of the instability

For $\Gamma = 1$ and $Gr = 0$ we find two types of instabilities, depending on the Prandtl number being either small ($Pr \lesssim 1$) or large ($Pr \gtrsim 1$).

4.1.1. Basic flow

The parabolic heat-flux profile on the free surface creates a non-uniform surface-temperature distribution which drives a surface flow away from the central hot region to the periphery via the thermocapillary effect. Due to continuity a return flow arises in the bulk, thus creating a toroidal vortex.

Streamlines and isotherms of the basic state for $Pr = 0.03$ are shown in figure 4(a) for critical conditions ($Re_c = 3.88 \times 10^4$). The basic vortex is attached to the free surface where the flow is driven and it is displaced towards the cold wall due to inertia effects. The flow in the lower half of the pool is separated forming a large weak secondary vortex. The basic temperature field is almost conducting at this low value of the Marangoni number $Ma^* = O(10)$ (see § 3). The Nusselt number is slightly less than unity, since the radial outward flow increases the mean surface temperature \bar{T} as compared to the mean conductive surface temperature \bar{T}_0 (2.6).

Representative of moderate Prandtl numbers we consider $Pr = 4$. The basic state at criticality is shown in figure 4(b). The critical Reynolds number $Re_c = 1.10 \times 10^5$ is about three times larger than for $Pr = 0.03$. The toroidal vortex does not differ much from the one at $Pr = 0.03$, but it extends deeper into the pool and flow separation arises only close to the corner made by the bottom and the side wall. Owing to the increased convective transport the isotherms are significantly compressed towards the free surface and towards the sidewall next to the cold corner. The central part of the free surface is significantly cooled by the strong convection which transports cold fluid vertically upwards the free surface. As a result the mean surface temperature is reduced and the Nusselt number $Nu = 4.86$ is large.

4.1.2. Stability boundaries

Neutral stability boundaries for $\Gamma = 1$ and $Gr = 0$ have been computed for wave numbers $m = 1-7$. Out of these the most dangerous ones are $m = 2, 3$ and 4. The corresponding neutral curves are shown in figure 5(a). Two ranges can be distinguished. For low Prandtl numbers ($Pr \lesssim 1$) the basic flow is unstable to a stationary mode with wavenumber $m = 2$ or 3, depending on the Prandtl number. Calculations for $Pr = 10^{-10}$ (cf. § 4.2.1) confirmed that the asymptotic range for $Pr \rightarrow 0$ is reached for $Pr \lesssim 0.01$.

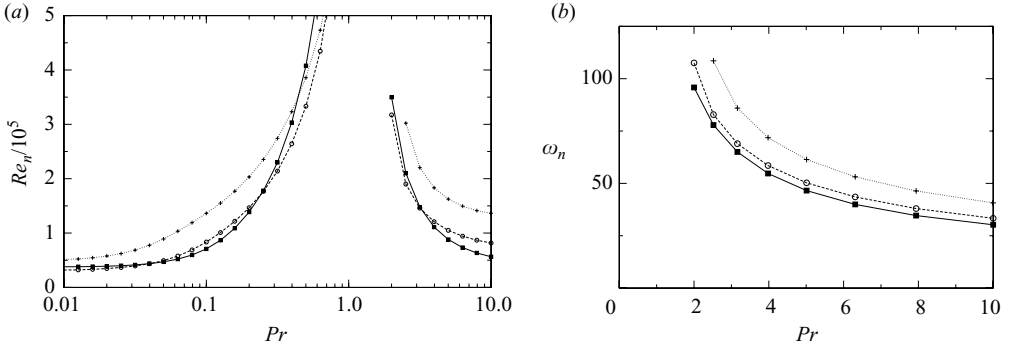


FIGURE 5. Neutral Reynolds numbers (a) (logarithmic scale) and neutral frequencies (b) (linear scale) for $\Gamma = 1$ and $Gr = 0$. The wave numbers are $m = 2$ (full line, ■), $m = 3$ (dashed line, ○) and $m = 4$ (dotted line, +).

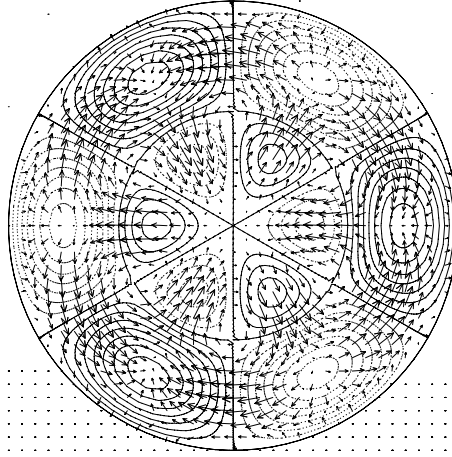


FIGURE 6. Critical flow (arrows) and temperature field (isolines) on the free surface $z = 0.5$ for $\Gamma = 1$, $Pr = 0.03$, $m = 3$ and $Re_c = 3.88 \times 10^4$. Negative temperatures are indicated by dotted lines.

For moderate Prandtl numbers ($Pr \gtrsim 1$) a Hopf bifurcation occurs to an oscillatory flow with wavenumber $m = 2$ or 3 depending on Pr . The neutral frequencies ω_n are displayed in figure 5(b). The neutral Reynolds numbers for $Pr \gtrsim 1$ are $O(10^5)$.

4.1.3. Low-Prandtl-number instability mechanism

The stationary instability for $Pr = 0.03$ occurs at $Re_c = 3.88 \times 10^4$ with wavenumber $m = 3$. Figure 6 shows the critical mode at the free surface $z = 0.5$. The temperature perturbations are very weak for this low Prandtl number. The critical mode exhibits a ring of weak surface-temperature extrema near the axis and a second somewhat stronger ring of extrema near the rim of the pool. The radial surface flow between the inner and the outer extrema is consistent with the thermocapillary effect, i.e. the radial perturbation flow and the surface forces caused by the perturbation-temperature field are essentially parallel ($\gamma > 0$). The azimuthal perturbation flow between adjacent outer and stronger temperature extrema, however, is oriented antiparallel to the azimuthal thermocapillary stress. Hence, the azimuthal motion cannot be created by the thermocapillary effect. In the absence of buoyancy forces such a perturbation flow

Pr	Γ	Re_c	m	Nu	I_v	I_v^-	I_v^+	M	δE_{kin}
0.03	1	3.88×10^4	3	0.96	1.013	0.714	0.299	-0.002	0.011
4	1	1.10×10^5	2	4.86	0.065	0.068	-0.003	0.982	0.047
10^{-10}	2	3.34×10^4	7	1.00	1.023	0.721	0.302	0.000	0.023
10^{-10}	4.5	1.28×10^5	4	1.00	1.030	0.654	0.376	0.000	0.030

TABLE 1. Kinetic energy budget of the critical mode according to (2.13) for selected cases ($Gr = 0$).

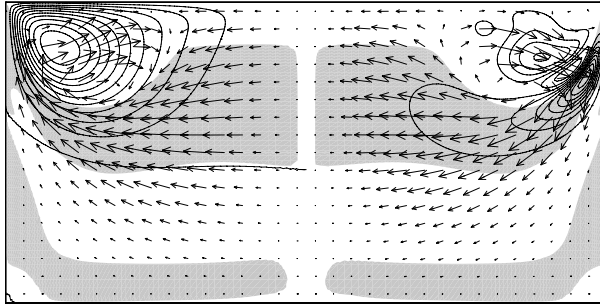


FIGURE 7. Vertical cross-section for $\Gamma = 1$, $Gr = 0$, $Pr = 0.03$, $m = 3$ and $Re_c = 3.88 \times 10^4$ showing the critical mode (vectors) at an azimuthal angle for which the total local production i_v takes its maximum. Also shown are basic-state streamlines (a) and isolines of i_v (b). Regions within which $\Phi(r) < 0$ are grey-shaded.

should be driven by inertial effects. This hypothesis is supported by the kinetic energy balance (table 1) which shows that the kinetic energy production I_v is the dominating destabilizing process. The integral contribution M of the Marangoni stresses for $Pr = 0.03$ is vanishingly small compared I_v and it even acts stabilizing.

For the inertial instability of the axisymmetric toroidal thermocapillary vortex flow in low-Prandtl-number liquid bridges Nienhüser & Kuhlmann (2002) have shown that vortex straining as well as centrifugal effects destabilize the basic flow (for the lid-driven cavity, see Albensoeder, Kuhlmann & Rath 2001). We argue that the centrifugal mechanism is dominating for the present low-Prandtl-number instability for $\Gamma = 1$. To that end we refer to the generalized Rayleigh criterion of Bayly (1988) which ascertains that the flow of an inviscid fluid is centrifugally unstable if a closed convex streamline exists all along which the magnitude of the circulation decreases outwards. According to the formulation by Sipp & Jacquin (2000) a two-dimensional inviscid flow is centrifugally unstable if

$$\Phi(r) := \frac{|u_0| \Omega_0}{\mathcal{R}} < 0 \quad (4.1)$$

all along a closed convex streamline. Here Ω_0 is the vorticity of the basic flow and \mathcal{R} the local radius of curvature of the streamline. Even though the criterion is valid for *inviscid* flows only, we have evaluated (4.1) for the present *viscous* basic flow. The result is shown in figure 7.

The criterion (4.1) holds true in the grey-shaded areas. Most notably, the regions which would favour a centrifugal instability in an inviscid flow are aligned with the outer streamlines of the basic toroidal vortex (figure 7a). The region extends from the cold corner where the accelerated free-surface flow is deflected downwards and along

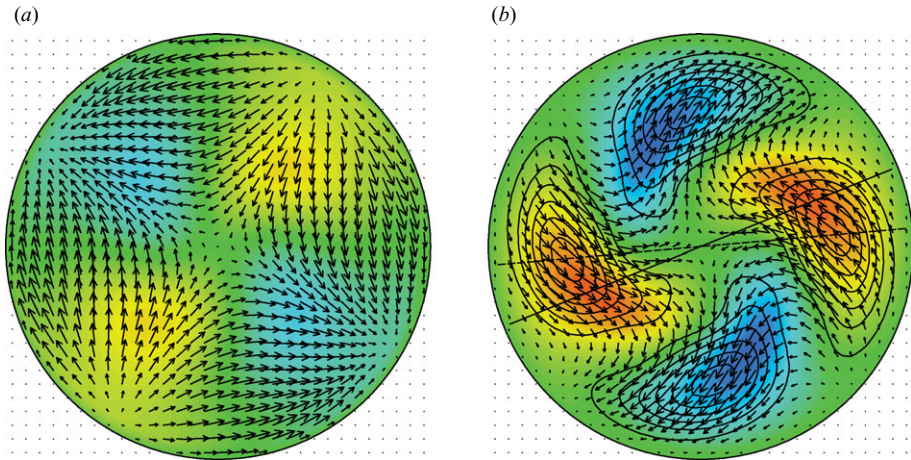


FIGURE 8. Critical flow (arrows) and temperature field (colour) at $Re_c = 1.10 \times 10^5$ with $m = 2$ and $\omega_c = 54.54$ for $Pr = 4$, $\Gamma = 1$ and $Gr = 0$. Shown is (a) the free surface at $z = 0.5$ and (b) the midplane at $z = 0$. The local thermal energy production i_T is shown by isolines in (b). The straight solid line indicates the azimuthal angle of the two internal temperature maxima (the corresponding vertical cut is shown in figure 9a). The straight dashed line indicates the azimuthal angle of the thermal production extrema (cf. figure 9b). The critical mode rotates clockwise.

the sidewall until it separates and turns radially inwards at about mid-height of the pool. The local production rate of kinetic energy i_v has a strong peak well within the region in which (4.1) is satisfied (figure 7b). If the local kinetic energy production i_v is decomposed into $i_v = i_v^- + i_v^+$, where i_v^- and i_v^+ represent the local production in the region where (4.1) holds and where (4.1) is not satisfied, respectively, I_v^- and I_v^+ being the corresponding integral rates (Shiratori, Kuhlmann & Hibiya 2007), then $I_v^- \gg I_v^+$ (table 1). Thus more than two thirds of the kinetic energy of the perturbation is produced in a region that would be subject to a centrifugal-type instability if the flow were inviscid. The mechanism of self-induced vortex straining due to the curvature of the vortex core that destabilizes, e.g. ring vortices (Widnall & Tsai 1977) seems to be of minor importance here, since the corresponding local peak of energy production near the centre of the vortex is relatively weak (figure 7).

We conclude that the low-Prandtl-number flow is unstable to a centrifugal instability. The critical mode and the region near the separation point where the kinetic energy production is peaked is very similar to the stationary centrifugal instability in deep lid-driven cavities (see figure 20 of Albensoeder *et al.* 2001).

4.1.4. Moderately high-Prandtl-number instability mechanism

For $Pr = 4$ the basic flow becomes unstable for $m = 2$ at $Re_c = 1.10 \times 10^5$ with $\omega_c = 54.54$. The perturbation temperature on the free surface $z = 0.5$ is shown in figure 8(a). Since the perturbation flow is directed from the hot to the cold perturbation-temperature spots, thermocapillary forces drive the perturbation flow. In fact, all other driving forces are insignificant. The kinetic energy production by inertia effects is vanishingly small compared to the Marangoni production ($I_v \ll M$, table 1).

For moderate and high Prandtl numbers, convection dominates over diffusion. Therefore, the surface spots could possibly be created by the vertical component of the perturbation flow which must arise due to continuity, similar as in the classical

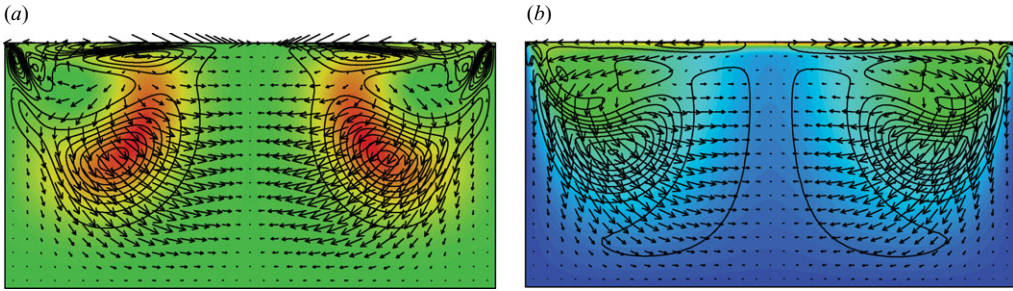


FIGURE 9. (a) Perturbation flow (arrows), perturbation temperature θ (colour) and local thermal production i_T (lines) in a vertical plane at an azimuthal angle for which the temperature perturbation takes its absolute maximum (solid line in figure 8b). (b) Perturbation flow (arrows), local thermal production (lines) and basic temperature field θ_0 (colour) in a vertical cut at an azimuthal angle for which the local thermal energy production takes its absolute maximum (dashed line in figure 8b). The colour scale from blue to red indicates temperatures from cold to hot, respectively. Parameters as in figure 8.

Marangoni problem (Pearson 1958). However, the Pearson mechanism cannot be at work here, because the vertical temperature gradient has the wrong sign: the free surface is hotter than the fluid below it (cf. figure 4b). The remaining possibilities are heat conduction and heat convection by the basic flow $\mathbf{u}_0 \cdot \nabla \theta$ from much stronger temperature extrema in the bulk. The latter process is more important for moderate Prandtl numbers and it is energy preserving in the integral sense. As figures 8(b) and 9(a) illustrate such bulk extrema do exist. They are created by thermal production caused by the thermocapillary-driven perturbation flow across the basic temperature isotherms. The perturbation temperature is then convected by the basic velocity field and finally reaches the free surface by conduction. The extrema of the local thermal production rate i_T arise azimuthally slightly ahead of those of the bulk temperature extrema. This is indicative of the clockwise rotation of the wave and consistent with the negative phase velocity which, for $m > 0$ and together with (2.11), is determined by the positive critical angular frequency $\omega_c = 54.54 > 0$ for the case presented. The different azimuthal angles are indicated by the full and dashed lines in figure 8(b). The respective vertical cuts are shown in figure 9(a, b).

The mechanisms discussed is identical with the one for hydrothermal waves in plane thermocapillary layers (Smith & Davis 1983) or in thermocapillary liquid bridges (Wanschura *et al.* 1995). We thus conclude that the moderately high-Prandtl-number instability in thermocapillary pools is due to hydrothermal waves.

4.1.5. Prandtl number dependence of the kinetic energy budget

The kinetic energy budget for $\Gamma = 1$ and $Gr = 0$ at criticality is shown in figure 10 as a function of Pr . In the low-Prandtl-number range the instability mechanism is inertial (centrifugal) throughout, since I_v (I_v^-) dominates. As $Pr \uparrow 1$ the basic temperature field is convectively compressed towards the cold wall and the thermocapillary stresses become less effective in driving the basic vortex. As a result the basic flow is stabilized, similar as in liquid bridges (Wanschura *et al.* 1995). For intermediate Prandtl numbers the stabilization is partially compensated by cooperating Marangoni forces which are most significant for the $m = 2$ mode at $Pr \approx 0.2$ (figure 10).

In the moderately high-Prandtl-number range the Marangoni production M increases with Prandtl number. While there is a sizable amount of kinetic energy produced by inertial processes (I_v) for $Pr \approx 2$, their contribution decreases rapidly for

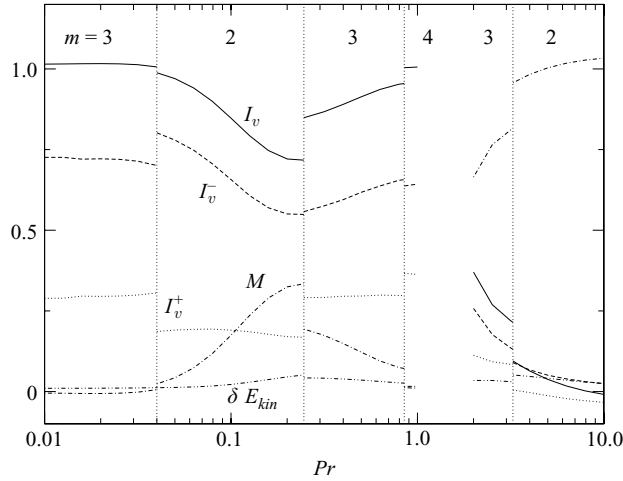


FIGURE 10. Budget of the kinetic energy (2.13) as function Pr for $\Gamma=1$ and $Gr=0$. The critical wavenumber is indicated at the top of the figure. The curves represent I_v (full line), I_v^- (dashed line), I_v^+ (dotted line), M (dash-dotted line) and the error δE_{kin} (dash-double-dotted line).

higher Prandtl numbers and may even act slightly stabilizing for $\Gamma=1$ and $Pr=10$. The thermal energy budget (2.17) is not of much interest, because it always represents an exact balance between thermal energy production and thermal diffusion. Similar as in liquid bridges the basic flow is stabilized for $Pr \downarrow 1$ due to the increase of thermal diffusion D_T compared to the convective transport of θ_0 and θ .

4.2. Aspect ratio dependence of the instability

4.2.1. Asymptotically small Prandtl numbers

In the limit of small Prandtl numbers $Pr \rightarrow 0$ the temperature field is exactly conducting and the dynamics is purely inertial. The conducting basic temperature field merely serves to drive the basic flow. For practical reasons we studied the behaviour for $Pr=10^{-10}$. This value is an excellent approximation of the zero-Prandtl-number limit if the Marangoni-Péclet number $Ma = Re Pr \ll 1$, i.e. if $Re \ll 10^{10}$. For the computed critical Reynolds numbers this condition is always satisfied and we find $Nu = 1.00$. Moreover, Re even overestimates the Reynolds number based on the actual flow velocities Re^* owing to the selected temperature scale (see §3).

The dependence on the aspect ratio of the basic flow at at criticality is displayed in figure 11. The diameter of the toroidal vortex scales with the smallest geometrical length scale available. For deep cavities $\Gamma \ll 1$ the diameter of the vortex in the (r, z) plane scales with the radius R . Hence, the flow does not significantly penetrate in axial direction. In the limit $\Gamma \rightarrow 0$ the toroidal vortex will drive a sequence of weak counter-rotating vortices stacked axially and decaying exponentially from the free surface (for rectangular thermocapillary cavities see Rybicki & Floryan 1987). For aspect ratios of order one and larger the vortex size scales with the depth. If Γ is large and the Reynolds number high a thin surface layer of fluid is accelerated towards the cold rim of the pool. On the cold wall the jet is deflected downwards forming a toroidal vortex. Where the upward return flow of the vortex impinges on the free surface and collides with the radial outward jet the excess fluid returns radially inwards. As a result, the flow at intermediate radial distances is nearly

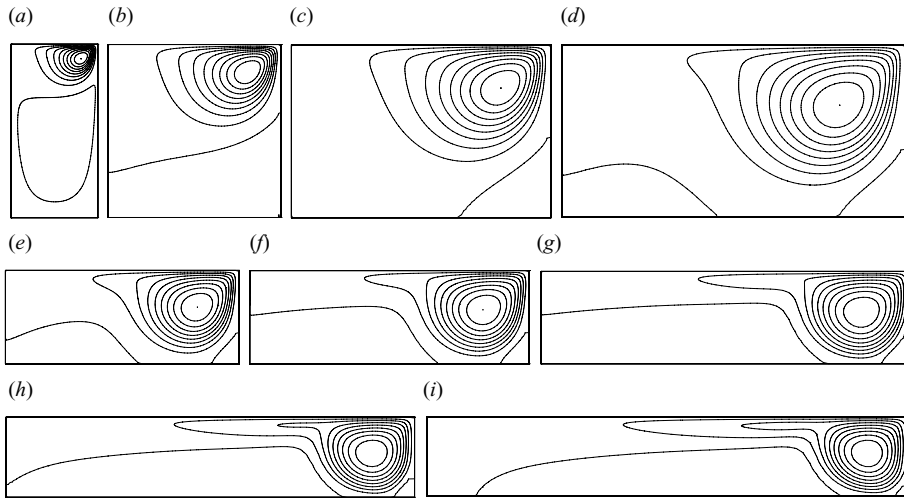


FIGURE 11. Basic-state stream function at criticality for $Pr = 10^{-10}$ and $Gr = 0$. The critical data (Γ, m_c, Re_c) are (a): $(0.5, 3, 1.15 \times 10^5)$, (b): $(1, 3, 2.91 \times 10^4)$, (c): $(1.5, 3, 2.02 \times 10^4)$, (d): $(2, 7, 3.34 \times 10^4)$, (e): $(2.5, 7, 3.54 \times 10^4)$, (f): $(3, 7, 6.70 \times 10^4)$, (g): $(4, 3, 1.21 \times 10^5)$, (h): $(5.1, 5, 1.43 \times 10^5)$ and (i): $(6.1, 7, 1.70 \times 10^5)$.

radial. Contrary to the low-Prandtl-number thermocapillary-driven flow in shallow rectangular domains (Ben Hadid & Roux 1990; Laure, Roux & Ben Hadid 1990), we did not find a horizontal sequence of co-rotating vortices decaying from the cold wall. This is most likely due to the type of heating by a free-surface heat flux and the cylindrical geometry.

Neutral curves and frequencies as function of Γ are shown in figure 12. In the range $\Gamma \lesssim 3.5$ neutral curves of several other modes (not shown) with different wavenumbers lie fairly close to, but above, the critical curves shown. Three ranges can be distinguished. For small aspect ratios $\Gamma \lesssim 1.91$ we find a stationary critical mode with a wavenumber $m = 3$. This is the same mode as for $\Gamma = 1$ which was discussed in §4.1.3 and which is destabilized by centrifugal effects. In the limit $\Gamma \rightarrow 0$, the depth d of the pool becomes irrelevant and the characteristic length scale is R . Since the length scale linearly enters $\Delta T \sim d$ as well as Re explicitly, the Reynolds number scales like $Re \sim d^2$. Hence we expect the asymptotic behaviour $Re_c \Gamma^2 = a$ as $\Gamma \rightarrow 0$. In fact, this scaling is found with $a = 2.8 \times 10^4$ (dash-dotted line in figure 12).

In the intermediate aspect-ratio range $1.91 \lesssim \Gamma \lesssim 3.31$ a qualitatively different type of instability arises. The critical wavenumber $m = 7$ is rather large and the normal mode is oscillatory. We consider the case $\Gamma = 2$ in more detail. The critical Reynolds number is $Re_c = 3.34 \times 10^4$ with $\omega_c = 157$. With $Pr = 10^{-10}$ the critical Marangoni number $Ma_c = Pr Re_c = 3.34 \times 10^{-6}$ is very small and the perturbation temperature field is irrelevant. Hence, the perturbation flow is entirely driven by inertial forces. This is confirmed by the kinetic energy budget (table 1). Evaluation of the Rayleigh criterion (4.1) yields the grey-shaded areas shown in figure 13(a). It is seen that one region in which (4.1) holds is aligned with the outer streamlines of the basic vortex, similar as in figure 7. The local kinetic energy production i_v is significantly peaked in that region and near the point of basic flow separation from the sidewall. Since most of the kinetic energy is produced in this region, we conclude that the instability is centrifugal in nature. Owing to the localization of the energy source the critical mode is confined to the region of the basic vortex and the perturbation flow is very

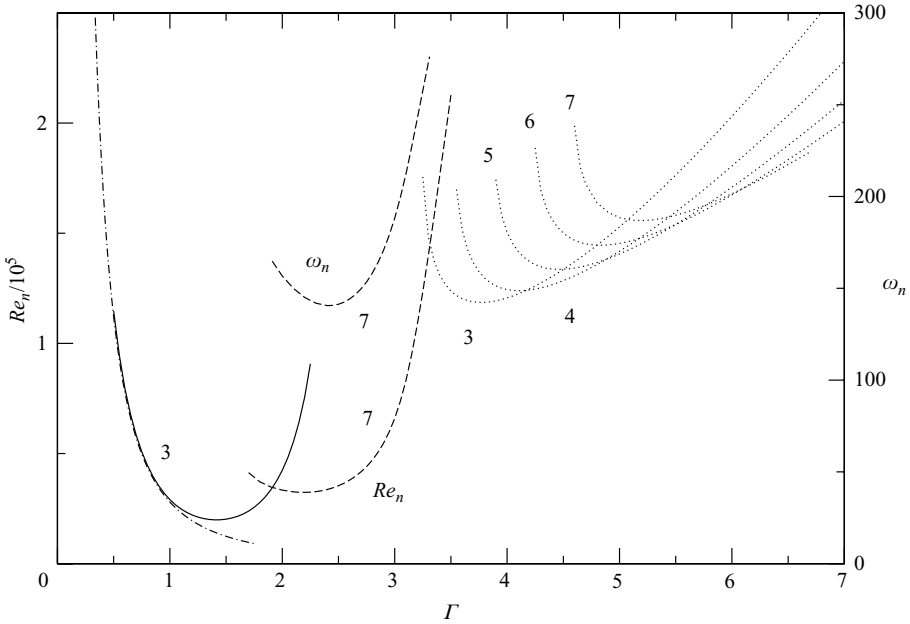


FIGURE 12. Critical Reynolds number as function of the aspect ratio for $Pr = 10^{-10}$ and $Gr = 0$. Numbers indicate the critical wavenumber m . The branches are stationary (full line, dotted lines) or oscillatory (dashed line). The upper dashed line represents the neutral frequency and the dash-dotted line is the asymptote $Re_c = 2.8 \times 10^4 / \Gamma^2$ for $\Gamma \rightarrow 0$.

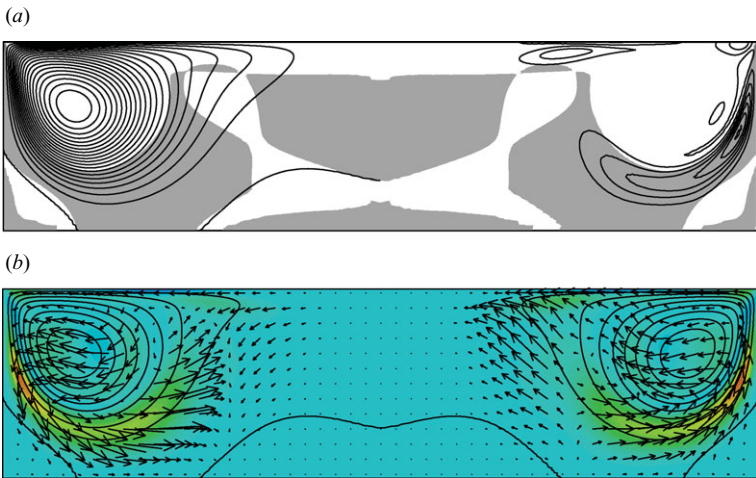


FIGURE 13. Vertical cross-section at an angle for which i_v takes its absolute maximum. The parameters are $Pr = 10^{-10}$, $\Gamma = 2$, $Gr = 0$, $m = 7$ and $Re_c = 3.34 \times 10^4$. (a) Regions (grey) in which the local Rayleigh criterion $\Phi(r) < 0$ holds. In addition, isolines of the basic-state stream function ψ_0 (left side) and isolines of i_v (right side) are shown. (b) Perturbation flow (arrows), i_v (colour) and ψ_0 (lines).

weak in the near-axis region of the pool (figure 13b). Figure 14 shows the critical flow field at four different horizontal layers. The Görtler-like vortices are best visible at $z = 0.25$ (figure 14b). While the kinetic energy production and the perturbation flow in the (r, z) plane is similar to the stationary small-aspect-ratio mode and the

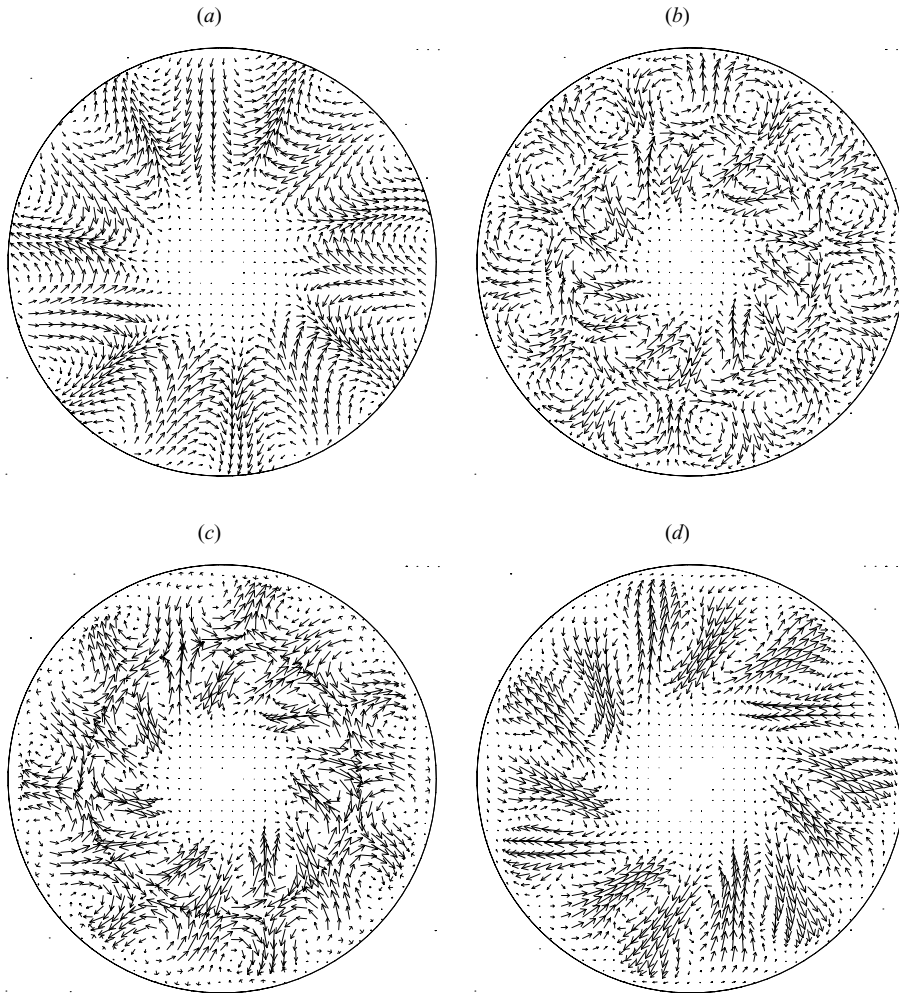


FIGURE 14. Critical flow for $\Gamma = 2$, $Pr = 10^{-10}$ and $Gr = 0$ at $Re_c = 3.34 \times 10^4$ with $\omega_c = 157$ and $m = 7$. Shown are horizontal planes at the free surface $z = 0.5$ (a), $z = 0.25$ (b), $z = 0$ (c) and $z = -0.25$ (d). The pattern rotates clockwise.

stationary mode in deep lid-driven cavities of Albensoeder *et al.* (2001), the present large-aspect-ratio mode is travelling azimuthally.

For even higher aspect ratios $\Gamma \gtrsim 3.31$ yet another type of instability is found. The critical perturbation is once again stationary and the critical wavenumber increases with the aspect ratio in regular steps of one. As a representative case for the high-aspect-ratio range we consider $\Gamma = 4.5$. The critical Reynolds number is $Re_c = 1.28 \times 10^5$ with $m = 4$. The critical mode at the free surface is shown in figure 15. Apart from a small zone near $r = 0$ and the rim $r = \Gamma$ the perturbation flow is nearly perfectly aligned in radial direction, not only on the free surface but also in the bulk. It is directed inwards in the regions of the (extremely weak) cold surface spots and outwards in the hot-spot regions (the perturbation temperature is not shown). The weak azimuthal surface flow near the rim is directed from the hot to the cold sectors.

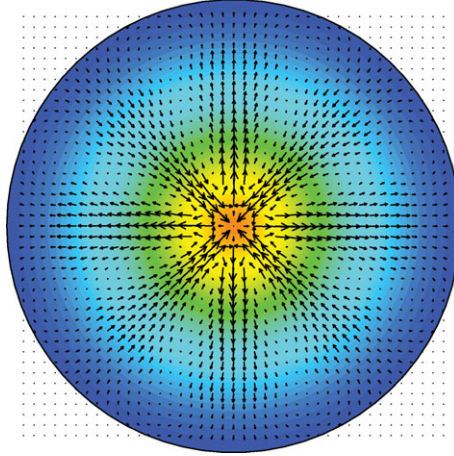


FIGURE 15. Critical flow with $m=4$ (arrows) and basic temperature field (colour) on the free surface $z=0.5$ at $Re_c = 1.28 \times 10^5$ for $\Gamma = 4.5$, $Pr = 10^{-10}$ and $Gr = 0$.

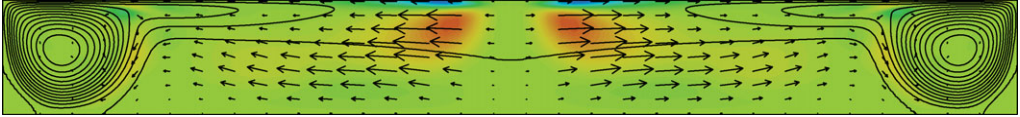


FIGURE 16. Vertical cut along the axis of the cylinder showing the perturbation flow (arrows), the total local production i_v (colour) and the basic stream function ψ_0 (lines). The cut is shown at an azimuthal angle at which i_v takes its absolute maximum. The parameters are $Pr = 10^{-10}$, $\Gamma = 4.5$, $Gr = 0$, $m = 4$ and $Re_c = 1.28 \times 10^5$.

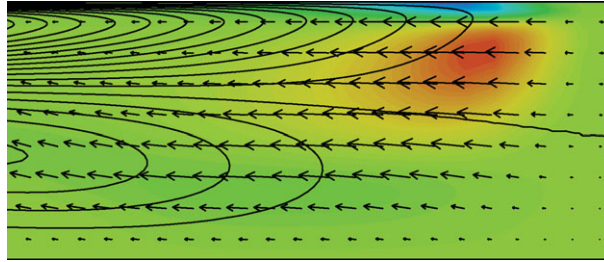


FIGURE 17. Close-up of figure 16 showing $-u^2 \partial_r u_0 / D$ (colour) instead of $i_v = -\mathbf{u} \cdot (\mathbf{u} \cdot \nabla \mathbf{u}_0) / D$.

The kinetic energy budget (table 1) shows that the instability is purely inertial. The main contribution to the kinetic energy production arises near the cylinder's axis in the upper half of the pool (figure 16). The figure shows the total local production $i_v = -\mathbf{u} \cdot (\mathbf{u} \cdot \nabla \mathbf{u}_0) / D$. The dominant contribution to the total production, however, is due to the term $-u^2 \partial_r u_0 / D$ which represents the local transfer rate of kinetic energy between the radial momentum of the basic flow u_0 and the radial velocity u of the perturbation flow. The latter production term is shown close-up in figure 17. It is nearly indistinguishable from i_v as in figure 16. To explain this production peak we note that the radial component u_0 of the basic flow has a local minimum (inward flow) at about $(r, z) = (0.65 \Gamma, 0.31)$. From this location the radial inward flow ($u_0 < 0$) increases monotonically to zero at $r = 0$. The basic radial inward

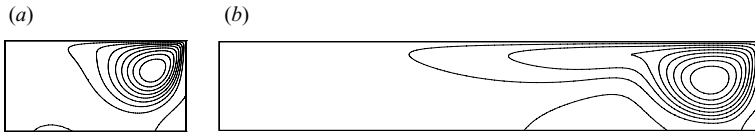


FIGURE 18. Basic-state stream function at criticality for $Pr = 0.03$ and $Gr = 0$. (a) $\Gamma = 2$, $Re_c = 2.84 \times 10^4$, $m = 3$. (b) $\Gamma = 6.1$, $Re_c = 4.51 \times 10^4$, $m = 6$.

flow is thus *decelerated* as the axis is approached. This deceleration despite of the cylindrical geometry is made possible by a strong entrainment of the inward flow by the rapid radial outward flow which arises in a very thin surface layer visible from the streamlines shown in figure 17. Since the kinetic energy production peak is located in the region of radial inward flow deceleration ($u_0 < 0$, cf. figure 17), we conclude that the instability is caused by the strong deceleration ($\partial_r u_0 < 0$) of the basic radial inward flow. All other production terms are much smaller. The instability thus is a property of the converging and decelerating near-axis subsurface flow which is made possible by the entrainment effect provided by the radial outward thermocapillary surface flow.

The instability at $\Gamma = 4.5$ shares some similarities with the flow observed in shallow pools driven by a point source of solute which locally reduces the surface tension. Such an experiment was first described by Thomson (1855). As reported by Shtern & Hussain (1993) similar experiments were conducted by Pshenichnikov & Yatsenko (1974). Small amounts of alcohol have been fed to the centre of the surface of water filled in a shallow dish. Driven by solutal gradients the axisymmetric flow was found to be unstable to azimuthal perturbations consisting of alternating radial inward and outward jets observable on the free surface of the liquid, very much like the pattern in figure 15. To better understand the instability one might consider the simplification of plane flow as in, e.g. Goldshtik, Hussain & Shtern (1991). Energy transfer from a basic source/sink flow $\mathbf{u}_0 = u_0(r)\mathbf{e}_r$ based on the *diverging* nature, i.e. the dependence on φ of the direction of the flow, would be $-\mathbf{u} \cdot [\mathbf{u} \cdot (r^{-1}\mathbf{e}_\varphi \partial_\varphi)\mathbf{u}_0] = -r^{-1}v^2 u_0$, which requires an azimuthal perturbations flow v . But this is not the case for the instability of plane source/sink flow nor for the present case. The energy-transfer mechanism in plane source/sink flow as well as in the present case relies on the deceleration/acceleration of the basic radial flow via the production rate $-u^2 \partial_r u_0$. Production is positive only for $\partial_r u_0 < 0$, i.e. for flow deceleration. This is realized in plane *diverging* source flow $u_0 \sim r^{-1}$ of an incompressible fluid. The same mechanism is operative in shallow thermocapillary pools of asymptotically small Prandtl number and we conclude that the instability is of the same nature as the one of a plane source flow.

4.2.2. $Pr = 0.03$

The low-Prandtl-number instability for $\Gamma = 1$ and its dependence on the Prandtl number has been discussed in §4.1, focusing on $Pr = 0.03$. Here we consider the dependence on the aspect ratio for $Pr = 0.03$. As can be seen from figure 18 the basic-state streamlines are similar to those for $Pr = 10^{-10}$. However, as the aspect ratio increases beyond $\Gamma \gtrsim 2$ Marangoni effect become significant in the instability mechanism. This effect is due to the increase of the Prandtl number from 10^{-10} to 0.03. As a result the flow is significantly destabilized as compared to $Pr = 10^{-10}$. This is seen from the neutral curves shown in figure 19 as compared to figure 12. Apparently, both the oscillatory mode and the high-aspect-ratio stationary modes ($Re_c \gtrsim 1.2 \times 10^5$) are superseded for $Pr = 0.03$ by stationary modes ($Re_c \lesssim 0.4 \times 10^5$)

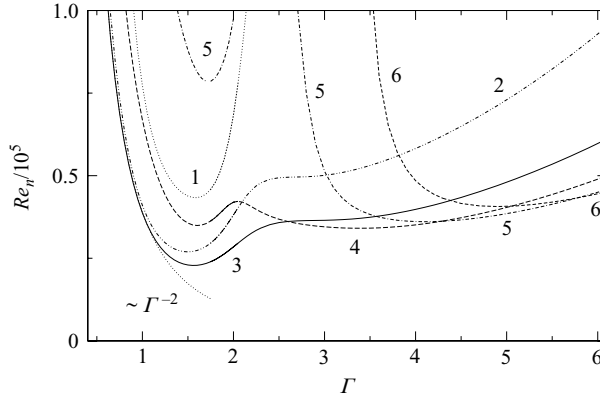


FIGURE 19. Neutral Reynolds numbers as functions of Γ for $Pr = 0.03$ and $Gr = 0$. The neutral wavenumbers m are indicated by labels. The dotted line in the lower left represents the asymptote $Re_c = 3.9 \times 10^4 / \Gamma^2$.

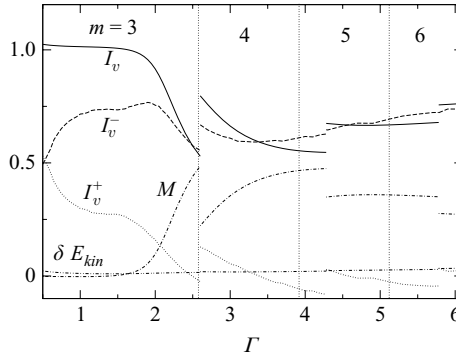


FIGURE 20. Kinetic energy budget as function of Γ for $Pr = 0.03$ and $Gr = 0$. The critical wavenumbers are indicated at the top of the figure. The curves represent I_v (full lines), I_v^- (dashed lines), I_v^+ (dotted lines), M (dash-dotted lines) and the error δE_{kin} (dash-double-dotted lines).

which have a structure similar to the small-aspect-ratio mode for $Pr = 10^{-10}$. As argued before, the critical Reynolds number should scale like $Re_c = a/\Gamma^2$ for $\Gamma \rightarrow 0$. We find $a = 3.9 \times 10^4$ (dotted line in figure 19).

The importance of the Marangoni production large aspect ratios Γ can be seen from figure 20. Yet, the major energy production remains due to centrifugal effects, similar as for $\Gamma = 1$ (figure 7). This conclusion is based on the dominating contribution of I_v^- to the total integral production $I \approx I_v^-$ for $\Gamma \gtrsim 2$ (figure 20). The significance of Marangoni forces is reflected by the velocity and temperature perturbation fields on the free surface shown in figure 21. For large Γ (figure 21d,e,f) the surface flow is mainly azimuthal and augmented by the thermocapillary effect induced by the sectorial perturbation temperature field. For decreasing Γ (figure 21a,b,c) additional temperature extrema arise near the rim of the pool, grow larger as Γ is decreased and even become dominant. The azimuthal thermocapillary effect due to the peripheral temperature spots is counteracting the azimuthal surface flow which reflects the dominance of inertial production as $\Gamma \rightarrow 0$.

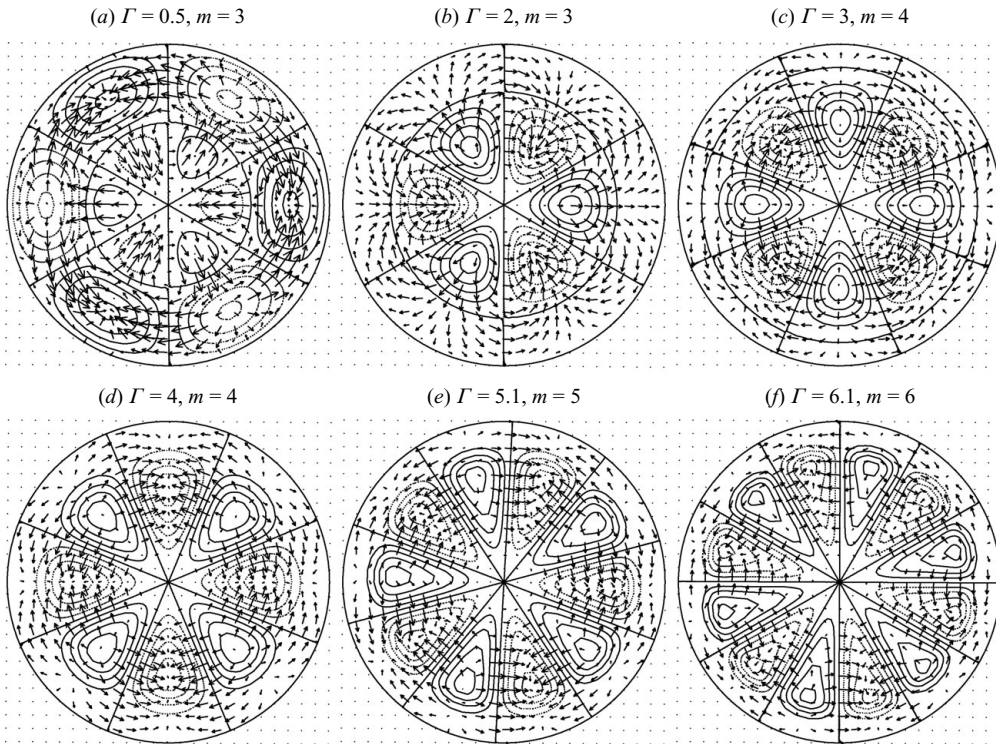


FIGURE 21. Critical perturbation flow (arrows) and temperature (lines) on the free surface $z=0.5$ for $Pr=0.03$ and $Gr=0$. Negative temperatures are indicated by dotted lines. The critical Reynolds numbers and Nusselt numbers (Re_c, Nu) are (a) $(1.55 \times 10^5, 0.965)$, (b) $(2.84 \times 10^4, 0.965)$, (c) $(3.45 \times 10^4, 0.963)$, (d) $(3.51 \times 10^4, 0.946)$, (e) $(3.90 \times 10^4, 0.932)$, (f) $(4.51 \times 10^4, 0.924)$.

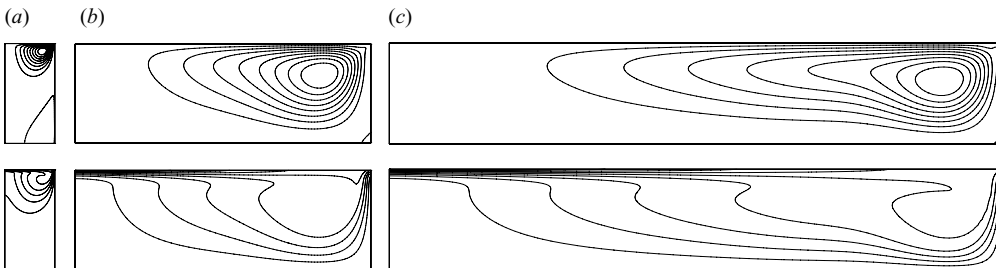


FIGURE 22. Basic-state stream function ψ_0 (upper row) and temperature field θ_0 (lower row) at criticality for Prandtl number $Pr=4$ and $Gr=0$. The parameters are (a) $\Gamma=0.5$, $Re_c=4.72 \times 10^5$, $m=2$, $Nu=5.02$; (b) $\Gamma=3$, $Re_c=5.99 \times 10^4$, $m=4$, $Nu=4.56$; (c) $\Gamma=6.1$, $Re_c=1.29 \times 10^5$, $m=6$, $Nu=4.01$.

4.2.3. $Pr=4$

Basic flow and temperature fields at the critical point for $Pr=4$ are provided in figure 22. Since the convective effect is much stronger for moderate Prandtl numbers as compared to smaller ones, the basic velocity fields at criticality are much weaker. Hence, the nearly fly-wheel inertial vortices (like figure 11*i*) cannot be found.

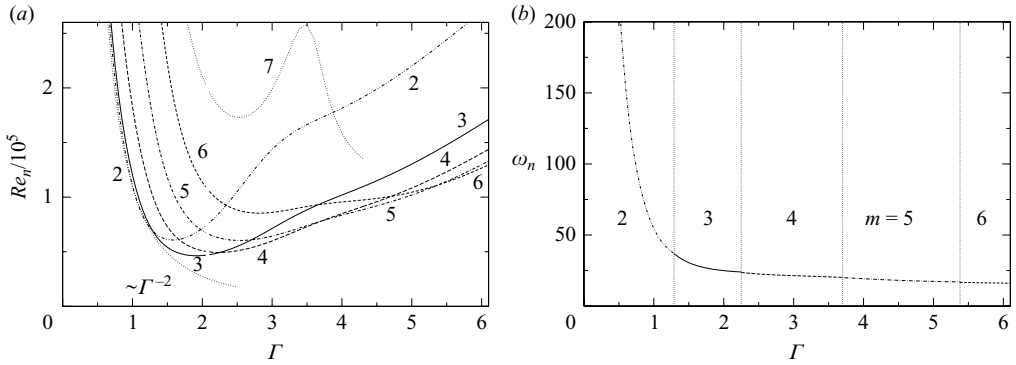


FIGURE 23. Aspect ratio dependence of the neutral Reynolds number Re_n (a) and neutral frequency ω_n (b) for $Pr = 4$ and $Gr = 0$. Wavenumbers m are given as labels. The asymptotic curve (dotted in (a)) is $Re_c = 1.1 \times 10^5 / \Gamma^2$.

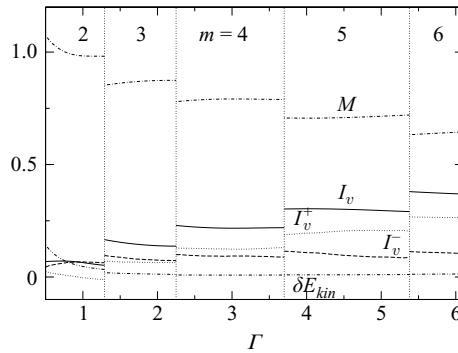


FIGURE 24. Kinetic energy budget for $Pr = 4$ and $Gr = 0$ as function Γ . The critical wavenumber is indicated at the top of the figure. The curves represent I_v (full line), I_v^- (dashed line), I_v^+ (dotted line), M (dash-dotted line) and the error δE_{kin} (dash-double-dotted line).

Neutral curves for $Pr = 4$ as functions of Γ are shown in figure 23(a). The critical modes are oscillatory for all wavenumbers m . The critical Reynolds number scales like $Re_c = 1.1 \times 10^5 / \Gamma^2$ as $\Gamma \rightarrow 0$. A scaling $\sim \Gamma^{-2}$ is also found for the oscillation frequency ω_c which is displayed in figure 23(b). The frequency does not suffer major jumps at the codimension-two points, i.e. the frequency is not determined by m . Obviously it is determined by the basic flow, more precisely by a suitably defined eddy-turn-over time (see e.g. Leypoldt, Kuhlmann & Rath 2000).

The aspect ratio dependence of the kinetic energy balance (2.13) is displayed in figure 24. As discussed in §4.1 the instability is mainly caused by the hydrothermal-wave mechanism. For all aspect ratios Marangoni forces are dominant in driving the perturbation flow. As Γ increases, and with it the critical wavenumber, inertial processes become increasingly effective in feeding kinetic energy to the perturbation flow. The relative importance of inertial to Marangoni production remains almost constant for a given wavenumber. If the tendency is extrapolated the instability might possibly be dominated by inertial production for sufficiently high aspect ratios.

$Pr = 10^{-10}$					$Pr = 10$					
Figure	Gr	Re_c	Bd	m	Figure	Gr	Re_c	Bd	m	Nu
25a	2.90×10^3	2.90×10^4	0.1	3	26a	5.69×10^3	5.69×10^4	0.1	2	5.27
25b	2.84×10^4	2.84×10^4	1	3	26b	5.97×10^4	5.97×10^4	1	2	5.39
25c	1.76×10^5	2.79×10^4	6.31	3	26c	5.53×10^5	8.76×10^4	6.31	2	5.74
25d	1.19×10^6	1.51×10^3	794	2	26d	3.53×10^6	2.81×10^5	12.6	1	7.25

TABLE 2. Parameters for figures 25 and 26. The dynamic Bond number is defined as $Bd = Gr/Re$. Data have been rounded to three significant decimals. For $Pr = 10^{-10}$ always $Nu = 1.00$.

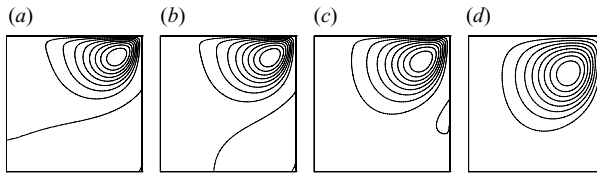


FIGURE 25. Basic-state stream function at criticality for $Pr = 10^{-10}$, $\Gamma = 1$ and increasing buoyancy (from (a) to (d)). The parameters are given in table 2.

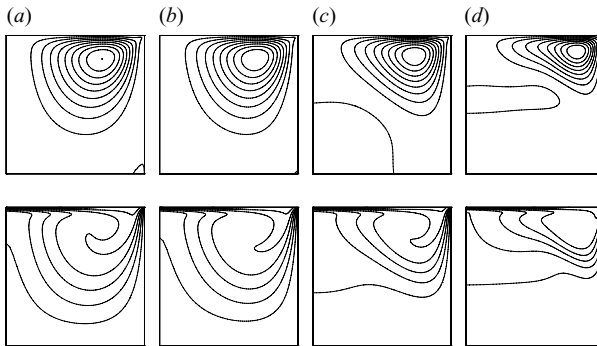


FIGURE 26. Basic-state stream function and temperature fields at criticality for $Pr = 10$, $\Gamma = 1$ and increasing buoyancy (from (a) to (d)). The parameters are given in table 2.

4.3. The influence of buoyancy

To discuss the effect of buoyancy we consider a liquid pool with $\Gamma = 1$ for asymptotically small and a high Prandtl number, i.e. for $Pr = 10^{-10}$ and $Pr = 10$, respectively.

Figure 25 (the parameters are given in table 2) shows a sequence of stream-function isolines for increasing Bond number $Bd = Gr/Re$. Buoyancy forces are directed downwards in the vicinity of the cold sidewall. They cause an increase in size of the primary clockwise rotating vortex. The separation from the cold sidewall is delayed and even completely suppressed for sufficiently high Bd . For $Pr = 10^{-10}$ the temperature field is almost conducting as in figure 4(a) for $Gr = 0$.

For $Pr = 10$ (figure 26) the effect of buoyancy is more intricate. Increasing buoyancy promotes the formation of thermal stratification. Hot surface fluid is convected downwards near the cold sidewall, but cannot penetrate deep into the pool owing to upward buoyancy. The radial inward return flow continues to rise towards the

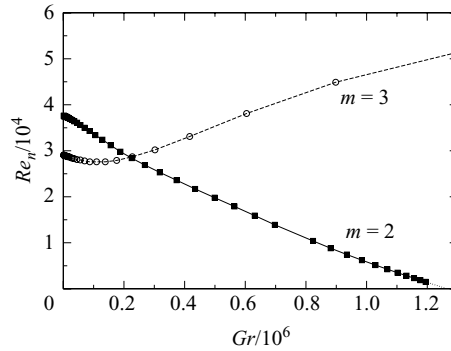


FIGURE 27. Grashof number dependence of the neutral Reynolds number Re_n for $\Gamma=1$ and $Pr=10^{-10}$.

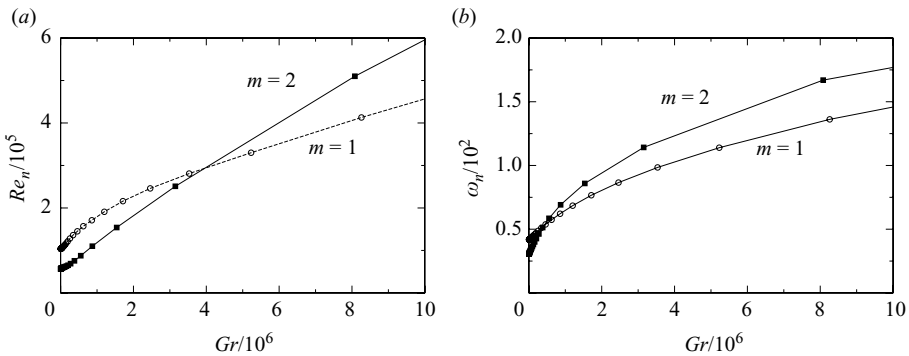


FIGURE 28. Grashof number dependence of the neutral Reynolds number Re_n (a) and frequency ω_n (b) for $\Gamma=1$ and $Pr=10$.

free surface. This leads to a flattening of the vortex resulting in a rounded triangular shape of the stream lines. Within the nearly stagnant lower part of the pool a weak counter-rotating ring vortex can arise as the remains of the larger separation zone in the lower half of the pool (figure 26d), reminiscent of vortex breakdown in swirling flows.

Figure 27 shows the dependence of the neutral Reynolds numbers on the Grashof number for $Pr=10^{-10}$ for the most dangerous modes. The critical parameters for $Pr=10$ are displayed in figure 28. The corresponding kinetic energy balances are shown in figure 29. Apart from a small range of Grashof numbers within which the most dangerous mode has $m=3$ the flow for $Pr=10^{-10}$ is destabilized by an $m=2$ mode for $Gr \gtrsim 2.2 \times 10^5$. Both thermocapillary and buoyancy forces drive the basic flow. They are, however, not important for the instability mechanism. As seen from figure 29(a) Marangoni production M is negligible for the kinetic energy budget within the full range of parameters. Buoyant production is even smaller ($|I_{Gr}| < 10^{-10}$). In the limit $Re \rightarrow 0$ the purely buoyancy-driven vortex becomes unstable at $Gr \approx 1.25 \times 10^6$ due to inertia. Figure 29(a) shows that no clear dominance of I_v^- nor I_v^+ can be found. The instability inertial mechanism depends on the details of the interaction between basic flow and critical mode.

For $Pr=10$ the basic flow is stabilized. The critical mode changes from $m=2$ to $m=1$ as Gr is increased. Obviously, the stabilization is due to the increasing thermal stratification of the basic flow (figure 26). The kinetic energy is primarily

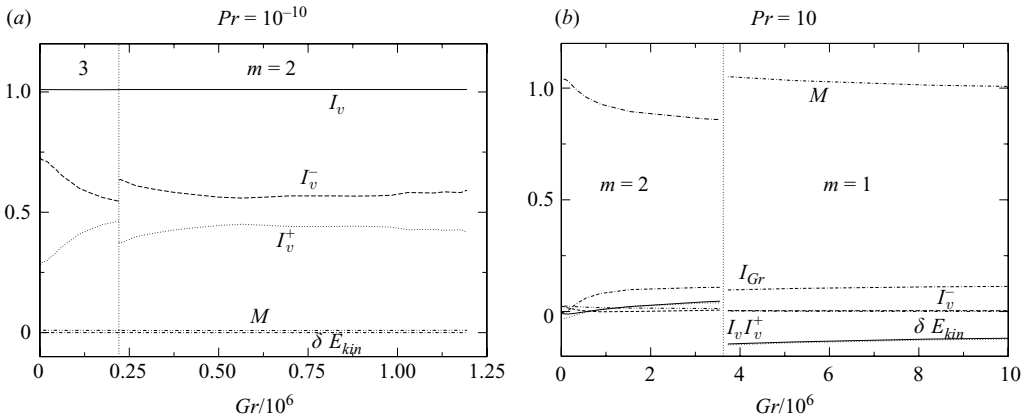


FIGURE 29. Kinetic energy budgets as function of Gr for $\Gamma = 1$ and $Pr = 10^{-10}$ (a) and $Pr = 10$ (b). The curves represent I_v (full lines), I_v^- (dashed lines), I_v^+ (dotted lines), M (dash-dotted lines), I_{Gr} (double-dash-dotted lines) and the error δE_{kin} (dash-double-dotted lines). I_{Gr} is practically zero for $Pr = 10^{-10}$ and has been omitted in (a).

produced by Marangoni production M , assisted by modest buoyancy production (figure 29b). These features, together with the oscillatory character of the critical mode are indicative of a hydrothermal wave. The increase of the critical threshold is associated with a structural change of the basic temperature field such that the critical mode becomes less efficient in extracting *thermal energy* from the basic state. Hence, higher Reynolds numbers are required to render the basic state unstable.

5. Summary

The basic thermocapillary flow in cylindrical liquid pools driven by an axisymmetric free-surface heat flux with a parabolic profile is characterized by a single vortex ring close to the cold corner made by the free surface and the outer wall. Different mechanisms can make the flow unstable to three-dimensional perturbations.

For $Gr = 0$ and moderately small Prandtl numbers centrifugal effects act destabilizing, similar as in the lid-driven cavity problem (Albensoeder *et al.* 2001) or in low-Prandtl-number thermocapillary liquid bridges (Nienhüser & Kuhlmann 2002). For moderately high Prandtl numbers, hydrothermal waves arise which gain thermal energy from internal basic-state temperature gradients (Smith & Davis 1983). Again, the same mechanism has been found in thermocapillary liquid bridges by Wanschura *et al.* (1995). Two other instabilities have been found for asymptotically small Prandtl numbers. These are the oscillatory centrifugal instability for intermediate aspect ratios ($1.92 \lesssim \Gamma \lesssim 3.31$) and a stationary instability for $\Gamma \gtrsim 3.31$. The latter instability is driven by a strong deceleration of the subsurface return flow as it approaches the axis. Buoyancy stabilizes the moderately high-Prandtl-number hydrothermal waves when gravity acts downwards ($Gr > 0$), whereas, for asymptotically small Prandtl number, buoyancy acts destabilizing, since it is augmenting the thermocapillary driving. In the limit for $\Gamma \rightarrow 0$ the basic flow becomes independent of the depth d of the pool. Hence, the critical Reynolds number $Re \sim d^2$ must asymptotically scale like $\sim \Gamma^{-2}$, since the radius R is the only relevant length scale. This behaviour was confirmed and quantified.

An open problem is the relation of the instability mechanism for shallow pools of very low-Prandtl-number fluids to the instability in solutocapillary pools (Thomson 1855; Pshenichnikov & Yatsenko 1974). To validate the hypothesis that the instability in solutocapillary pools is triggered in the converging subsurface flow further detailed analyses are required. One indication in support of this interpretation is the fact that the inertial production has a tendency to become more important for a fixed high Prandtl (Schmidt) number as the aspect ratio increases (figure 24). In addition to this issue and important for applications, it would be very interesting to study the effects of the heat flux profile, the pool geometry, motion in the gas phase, or the role of surfactants which can strongly influence the surface tension.

We gratefully acknowledge computing time provided by the Zentraler Informatik Dienst (ZID) of Vienna University of Technology.

REFERENCES

- ALBENSOEDER, S., KUHLMANN, H. C. & RATH, H. J. 2001 Three-dimensional centrifugal-flow instabilities in the lid-driven cavity problem. *Phys. Fluids* **13**, 121–135.
- BAYLY, B. J. 1988 Three-dimensional centrifugal-type instabilities in inviscid two-dimensional flows. *Phys. Fluids* **31**, 56–64.
- BEN HADID, H. & ROUX, B. 1990 Thermocapillary convection in long horizontal layers of low-Prandtl-number melts subject to a horizontal temperature gradient. *J. Fluid Mech.* **221**, 77–103.
- BOECK, T. & KARCHER, C. 2003 Low-Prandtl-number Marangoni convection driven by localized heating on the free surface: results of three-dimensional direct simulations. In *Interfacial Fluid Dynamics and Transport Processes* (ed. R. Narayanan & D. Schwabe), Lecture Notes in Physics, vol. 628, pp. 157–175. Springer.
- DEBROY, T. & DAVID, S. A. 1995 Physical processes in fusion welding. *Rev. Mod. Phys.* **67**, 85–112.
- GOLDSHTIK, M., HUSSAIN, F. & SHTERN, V. 1991 Symmetry breaking in vortex-source and Jeffery–Hamel flows. *J. Fluid Mech.* **232**, 521–566.
- GOLUB, H. G. & VAN LOAN, H. G. 1989 *Matrix Computations*. Johns Hopkins University Press.
- HINTZ, P., SCHWABE, D. & WILKE, H. 2001 Convection in a Czochralski crucible – part 1: non-rotating crystal. *J. Cryst. Growth* **222**, 343–355.
- HURLE, D. T. J. (Ed.) 1994 *Handbook of Crystal Growth*. North Holland.
- JING, C. J., IMAISHI, N., YASUHIRO, S. & MIYAZAWA, Y. 1999 Three-dimensional numerical simulation of spoke pattern in oxide melt. *J. Cryst. Growth* **200**, 204–212.
- KAMOTANI, Y., LEE, J. H. & OSTRACH, S. 1992 An experimental study of oscillatory thermocapillary convection in cylindrical containers. *Phys. Fluids A* **4**, 955–962.
- KAMOTANI, Y. & OSTRACH, S. 1994 Analysis of velocity data taken in surface tension driven convection experiment in microgravity. *Phys. Fluids* **6**, 3601–3609.
- KAMOTANI, Y., OSTRACH, S. & MASUD, J. 1999 Oscillatory thermocapillary flows in open cylindrical containers induced by CO₂ laser heating. *Intl J. Heat Mass Transfer* **42**, 555–564.
- KAMOTANI, Y., OSTRACH, S. & MASUD, J. 2000 Microgravity experiments and analysis of oscillatory thermocapillary flows in cylindrical containers. *J. Fluid Mech.* **410**, 211–233.
- KARCHER, CH., SCHALLER, R., BOECK, TH., METZNER, CH. & THESS, A. 2000 Turbulent heat transfer in liquid iron during electron beam evaporation. *Intl J. Heat Mass Transfer* **43**, 1759–1766.
- KUHLMANN, H. C. 1999 *Thermocapillary Convection in Models of Crystal Growth*, Springer Tracts in Modern Physics, vol. 152. Springer.
- KUHLMANN, H. C. & NIENHÜSER, C. 2002 Dynamic free-surface deformations in thermocapillary liquid bridges. *Fluid Dyn. Res.* **31**, 103–127.
- LAURE, P., ROUX, B. & BEN HADID, H. 1990 Nonlinear study of the flow in a long rectangular cavity subjected to thermocapillary effect. *Phys. Fluids A* **2**, 516–524.
- LEYPOLDT, J., KUHLMANN, H. C. & RATH, H. J. 2000 Three-dimensional numerical simulation of thermocapillary flows in cylindrical liquid bridges. *J. Fluid Mech.* **414**, 285–314.
- NIENHÜSER, C. & KUHLMANN, H. C. 2002 Stability of thermocapillary flows in non-cylindrical liquid bridges. *J. Fluid Mech.* **458**, 35–73.

- PEARSON, J. R. A. 1958 On convection cells induced by surface tension. *J. Fluid Mech.* **4**, 489–500.
- PSHENICHNIKOV, A. F. & YATSENKO, S. S. 1974 Convective diffusion from localized source of surfactant. *Hydrodynamics* **5**, 175–181 (in Russian).
- PUMIR, A. & BLUMENFELD, L. 1996 Heat transport in a liquid layer locally heated on its free surface. *Phys. Rev. E* **54**, R4528–R4531.
- RYBICKI, A. & FLORYAN, J. M. 1987 Thermocapillary effects in liquid bridges. I. Thermocapillary convection. *Phys. Fluids* **30**, 1956–1972.
- SCHIMMEL, F., ALBENSOEDER, S. & KUHLMANN, H. 2005 Stability of thermocapillary-driven flow in rectangular cavities. *Proc. Appl. Math. Mech.* **5**, 583–584.
- SCHWABE, D., ZEBIB, A. & SIM, B.-C. 2003 Oscillatory thermocapillary convection in open cylindrical annuli. Part 1. Experiments under microgravity. *J. Fluid Mech.* **491**, 239–258.
- SCRIVEN, L. E. & STERNLING, C. V. 1960 The Marangoni effects. *Nature* **187**, 186–188.
- SEN, A. K. & DAVIS, S. H. 1982 Steady thermocapillary flows in two-dimensional slots. *J. Fluid Mech.* **121**, 163–186.
- SHIRATORI, S., KUHLMANN, H. C. & HIBIYA, T. 2007 Linear stability of thermocapillary flow in partially confined half-zones. *Phys. Fluids* **19**, 044103-1–044103-19.
- SHTERN, V. & HUSSAIN, F. 1993 Azimuthal instability of divergent flows. *J. Fluid Mech.* **256**, 535–560.
- SIM, B.-C., KIM, W.-S. & ZEBIB, A. 2004 Axisymmetric thermocapillary convection in open cylindrical annuli with deforming interfaces. *Intl J. Heat Mass Transfer* **47**, 5365–5373.
- SIM, B.-C. & ZEBIB, A. 2002 Thermocapillary convection with undeformable curved surfaces in open cylinders. *Intl J. Heat Mass Transfer* **45**, 4983–4994.
- SIM, B.-C., ZEBIB, A. & SCHWABE, D. 2003 Oscillatory thermocapillary convection in open cylindrical annuli. Part 2. Simulations. *J. Fluid Mech.* **491**, 259–274.
- SIPP, D. & JACQUIN, L. 2000 Three-dimensional centrifugal-type instabilities of two-dimensional flows in rotating systems. *Phys. Fluids* **12**, 1740–1748.
- SMITH, M. K. & DAVIS, S. H. 1983 Instabilities of dynamic thermocapillary liquid layers. Part 1. Convective instabilities. *J. Fluid Mech.* **132**, 119–144.
- THOMSON, J. 1855 On certain curious motions observable at the surfaces of wine and other alcoholic liquors. *Lond. Edinburgh Dublin Phil. Mag. J. Sci.* **10**, 330–333.
- VILLERS, D. & PLATTEN, J. K. 1992 Coupled buoyancy and Marangoni convection in acetone: experiments and comparison with numerical simulations. *J. Fluid Mech.* **234**, 487–510.
- WANSCHURA, M., SHEVTSOVA, V. S., KUHLMANN, H. C. & RATH, H. J. 1995 Convective instability mechanisms in thermocapillary liquid bridges. *Phys. Fluids* **7**, 912–925.
- WIDNALL, S. E. & TSAI, CH.-Y. 1977 The instability of the thin vortex ring of constant vorticity. *Proc. R. Soc. Lond.* **287**, 273–305.
- XU, J.-J. & DAVIS, S. H. 1984 Convective thermocapillary instabilities in liquid bridges. *Phys. Fluids* **27**, 1102.